



ELSEVIER

Nuclear Instruments and Methods in Physics Research A 492 (2002) 212–235

**NUCLEAR  
INSTRUMENTS  
& METHODS  
IN PHYSICS  
RESEARCH**  
Section A

www.elsevier.com/locate/nima

# The performance of a novel ion-counting nanodosimeter

G. Garty<sup>a,\*</sup>, S. Shchemelinin<sup>a</sup>, A. Breskin<sup>a</sup>, R. Chechik<sup>a</sup>, G. Assaf<sup>a</sup>, I. Orion<sup>a</sup>,  
V. Bashkirov<sup>b</sup>, R. Schulte<sup>b</sup>, B. Grosswendt<sup>c</sup>

<sup>a</sup>Department of Particle Physics, Weizmann Institute of Science, Rehovot 76100, Israel

<sup>b</sup>Department of Radiation Medicine, Loma Linda University Medical Center, Loma Linda, CA 92354, USA

<sup>c</sup>Physikalisch-Technische Bundesanstalt (PTB), Braunschweig D-38116, Germany

Received 8 April 2002; accepted 7 May 2002

## Abstract

We present the performance of a novel device conceived for measuring minute energy deposits in a low-density gas, capable of operating in various radiation fields, including in an accelerator environment. The ion-counting nanodosimeter provides a precise measurement of the ionization distribution deposited within a small wall-less gas volume, modeling nanometer-scales of condensed matter, e.g. the DNA molecule. We describe the instrument and its data acquisition system. The results of systematic studies with low-energy alpha particles, protons and carbon ions are compared to model simulations; they demonstrate the capabilities and indicate the limitations of this novel technique. © 2002 Elsevier Science B.V. All rights reserved.

PACS: 87.53.Rd; 29.40.Cs; 61.80.-x

Keywords: Ion counting; Nanodosimetry; Radiation effects

## 1. Introduction

Measurements of ionization in gaseous models of condensed matter are the main tool in the field of radiation dosimetry [1]. These gas models substitute condensed matter with an equivalent gas, expanding the radiation interaction scale according to the density ratio, by factors of up to  $10^6$ , affording an insight into the process of radiation interaction with matter on microscopic scales. At such small scales, the energy deposition mechanism is highly stochastic, resulting in nano-

metric regions of condensed matter free of ionizations and others, containing a high density of ionizations (for example at the track ends of secondary electrons). Standard proportional counting techniques, based on integration of the charges over relatively large volumes, are therefore obviously inadequate tools for understanding the effects of this stochastic radiation action on very small targets.

This becomes especially true when looking at nanometric targets such as segments of the DNA molecule. It has been suggested [2], based on track structure modeling [3], that the relevant sub-cellular target for inducing irreparable damage is a cylinder of 2–4 nm diameter and 16 nm length, corresponding to a 50 base-pair segment of DNA

\*Corresponding author. Tel.: +972-8-934-2064; fax: +972-8-934-2611.

E-mail address: guy.garty@weizmann.ac.il (G. Garty).

and its surrounding water layer. Clustered radiation-induced lesions along this short segment of DNA have the potential of escaping the enzymatic repair mechanisms in the cell. It is therefore important to measure energy deposits in sensitive volumes corresponding to such small segments of DNA.

The nanometric clustering of radiation-induced ionizations can be evaluated by counting the number of charges deposited by radiation in a small volume of low-density gas, simulating the condensed matter target. This *nanodosimetric* measurement may permit quantifying the relative biological effectiveness (RBE) or a quality factor of a given radiation field with respect to a reference radiation of low linear-energy-transfer (LET). This is of prime importance in many fields including radiotherapy planning and radiation protection.

The clustering of ionizations may also be linked to fields other than biology. For example, nanodosimetry can also be applied to data corruption or device failure in microelectronic devices, placed in intense or complex radiation environments such as in high luminosity particle physics experiments or in space. The ongoing reduction in size of such devices, to nanometric scales, will seriously increase their susceptibility to radiation damage. Precise measurements of ionization clustering in gas models of sub-micron devices (such as a single transistor), may lead to the development of more radiation-hard electronics.

Several attempts were done to measure ionization clusters in nanometer-equivalent gas volumes. One approach uses counting of individual radiation-induced ionization electrons deposited in a low-pressure gas [4]. Though single electrons can be efficiently detected, electron diffusion at very low-gas pressures was found to seriously restrict the size of the model gas volume. Recent works based on this approach [5] refer to target sizes larger than 10 nm, although with rather low-detection efficiency, which could limit its use as a practical nanodosimeter. Another approach uses the optical visualization of electron avalanches along a particle track in low-pressure gas [6]. This method provides track-structure imaging with a time projection chamber recording avalanche-induced photons in a special “scintillating” gas.

The method permits attaining a tissue-equivalent resolution of 40 nm, but cannot resolve neighboring electrons along a track, due to the relatively broad individual electron avalanche spots. Here too, the electron diffusion limits the sensitivity of the method.

The diffusion limitation is overcome by recording positive ions rather than electrons. In an interesting concept, implemented by Pszona et al. [7], the nanometric target is simulated by an expanding gas jet confined within a small metal cell. The ions are counted after the gas has dissipated. Though the principle of the method has been demonstrated, the counting rate is limited, which makes it difficult to record rare, large-cluster events. “Wall-effects” in the small metal cell may also affect the measured results.

The idea of ion counting nanodosimetry was first introduced in Refs. [8,9], and further developed by us [10–13]. It is based on counting individual positive ions, induced by radiation in a small volume of low-pressure gas. These ions are extracted by an electric field, via a small orifice, into vacuum where they are accelerated onto a detector and counted. Similarly to the electron counting concept, the size of the equivalent gas volume is determined by the transport properties of ions within the gas enclosure, rather than by physical walls. This feature permits the conception of a wall-less sensitive volume (SV), eliminating undesired “wall-effects”. The SV size is tunable by a proper selection of gas, pressure and electric field geometry. Its maximal size, limited by the highest attainable pressure, is equivalent to a few tens to hundreds of nanometers in condensed matter. Nanometer-size sensitive volumes are obtained by reducing the gas pressure, and/or by applying some particular data analysis techniques, as described below. As no charge multiplication or scintillation mechanisms are required in the detection process, the method is not limited by the choice of gas.

In previous works we have described the ion-counting nanodosimeter (ND) concept in detail [11,12], and presented preliminary data [12–14] obtained with a nanodosimeter prototype. We present here a comprehensive description of the instrument and the experimental setup developed

by us for measuring ionization cluster size distributions in an accelerator environment. We present cluster size distributions obtained with monoenergetic thin beams of several radiation fields, in comparison with the results of model simulations. We provide a detailed account of the nanodosimeter performance and discuss its limitations and the validity of the measured data. The concept of combined physical and radiobiological measurements is discussed, as a possible way for assessing radiation damage to DNA. In this case the relevant nanodosimetric data have to be measured with broad beams, of a dimension much larger than the SV, in order to realistically simulate the geometry of a DNA segment under irradiation.

## 2. The ion-counting nanodosimeter

### 2.1. Nanodosimeter structure

A scheme of the ion-counting ND is shown in Fig. 1. A charged particle beam of a given type,

energy and geometry traverses an ionization volume (IV) and reaches a trigger detector. Ions induced in a wall-less sensitive volume (SV) within the IV are extracted into the vacuum-operated detection volume (DV) and are detected by an ion counter (IC).

The IV contains a low-pressure gas; in this work, we used propane at 0.9 Torr (a density of  $2.1 \times 10^{-6} \text{ g/cm}^3$ ). Under these conditions, 1 mm in gas corresponds to 2.1 nm at unit density. The IV is coupled by a 1 mm-diameter aperture to the intermediate vacuum region and to the DV, maintained at pressures of  $10^{-3}$  and  $3 \times 10^{-5}$  Torr respectively, by a double differential pumping system.

The size and shape of the wall-less SV are determined by the transport of ions in the gas and the spatial distribution of their extraction efficiency through the aperture. Ions deposited in proximity to the aperture are efficiently extracted from the IV, transported and detected by the IC. Those deposited at a distance from the aperture are extracted and detected with a lower efficiency. The SV size and shape can be tuned by varying the

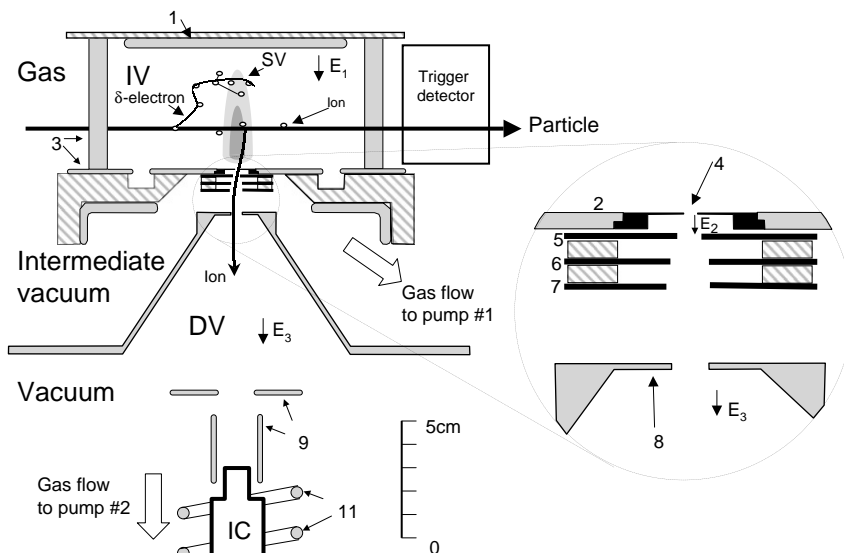


Fig. 1. A detailed diagram of the ion counting nanodosimeter construction. In the ionization volume (IV), the anode (1), cathode (2) and field shaping electrodes (3) determine the extraction field  $E_1$ . Ions created within the sensitive volume (SV) are extracted via the aperture (4) into the intermediate vacuum region; they are focused under the field  $E_2$ , via the electrodes  $A_1$  (5),  $A_2$  (6),  $A_3$  (7) and  $A_4$  (8) into the detection volume (DV). They are then accelerated and focused by the electrodes (9) into the ion counter (IC). A helical coil (11) protects the ion counter from discharges. Note that the SV and  $\delta$ -electron are schematic representations and not to scale.

gas density, the aperture diameter as well as the electric fields above and below the ion extraction aperture ( $E_1$  and  $E_2$  respectively).

The SV is represented by a map of tapered, cylindrically symmetrical volume-contours, corresponding to equal ion extraction efficiencies, as seen in Fig. 2. These efficiency maps were calculated for propane pressure of 0.9 Torr and electric field values of  $E_1 = 60$  V/cm and  $E_2 = 700$  or 1100 V/cm, using simulated electric field distributions in the ND and measured gas transport parameters of the ions [12]. The SV can be parameterized, for example, by the 50% ion extraction efficiency contour. In our selected conditions (Fig. 2b), this efficiency contour has a

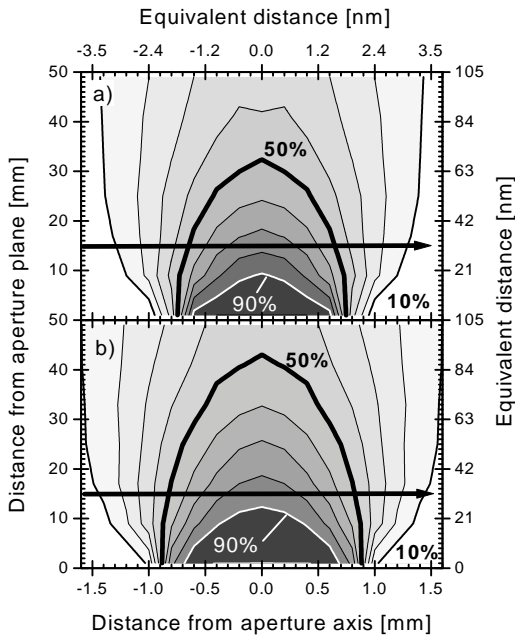


Fig. 2. Monte Carlo-simulated maps of the ion extraction efficiency from the ionization volume, defining the wall-less sensitive volume. Each contour line represents a change of 10% in the ion extraction efficiency. The arrow represents the location and diameter of the collimated beam in the present experiments. The bottom and left scales are real distances in gas, while the top and right scales provide the equivalent distances in tissue. The length of the 50% contour quoted in Fig. 13 and in the text is measured along the SV axis, while the width is measured at the base. Figure (a) corresponds to an electric field configuration:  $E_1 = 60$  V/cm,  $E_2 = 700$  V/cm and (b) corresponds to  $E_1 = 60$  V/cm,  $E_2 = 1100$  V/cm. Note a factor of  $\sim 15$  between vertical and horizontal scales.

diameter equivalent to 3.7 nm and a length equivalent to 90 nm, in unit density condensed matter. Smaller sensitive volumes can be easily reached by reducing the gas pressure or by applying ion arrival-time cuts on the raw data (see below). It should be noted that the size of the SV needs to be carefully chosen according to the application. Generally, in biological applications, the entire SV will be exposed to a geometrically broad radiation field, typically with a wide energy spectrum. In this work, for practical reasons, the characterization of the ND has been done with a monoenergetic pencil beam, having a diameter smaller than that of the SV. This permitted precise diagnosis of the nanodosimeter performance and comparison of the measured ionization distributions with that simulated by our Monte Carlo (MC) code. The dimensions of the SV chosen in this work do not necessarily correspond to the ideal size for any particular application but rather demonstrate the capability of the method to simulate sensitive volumes of nanometer dimensions.

It can be seen in Fig. 2 that the SV diameter is somewhat broader than the physical diameter of the aperture. This is due to ion focusing into the aperture, provided by the electric field  $E_2$ . Indeed, the two maps shown in Fig. 2 differ only by the choice of  $E_2$  values. The ion focusing effect can be clearly seen in Fig. 3, which depicts simulated single-ion trajectories in the case of strong focusing and without focusing.

The IV is enclosed in a stainless steel vessel of 150 mm diameter, much larger than the few-mm diameter SV. The electric field  $E_1$  is shaped by an aluminum anode, placed 50 mm above the grounded cathode encompassing the ion-extraction aperture. Additional field shaping electrodes ensure field uniformity.

The value of  $E_1$  largely defines the length of the SV. However, it was measured that when  $E_1$  is larger than 40 V/cm at  $\sim 1$  Torr propane, ionization electrons, induced in the gas by the projectile particle, may induce further ionizations en route to the anode, generating additional ions. In order to avoid this effect, we apply a pulsed electric field  $E_1$ , using a high voltage pulser (Directed Energy Inc. model GRX). A constant background field  $E_1$  is

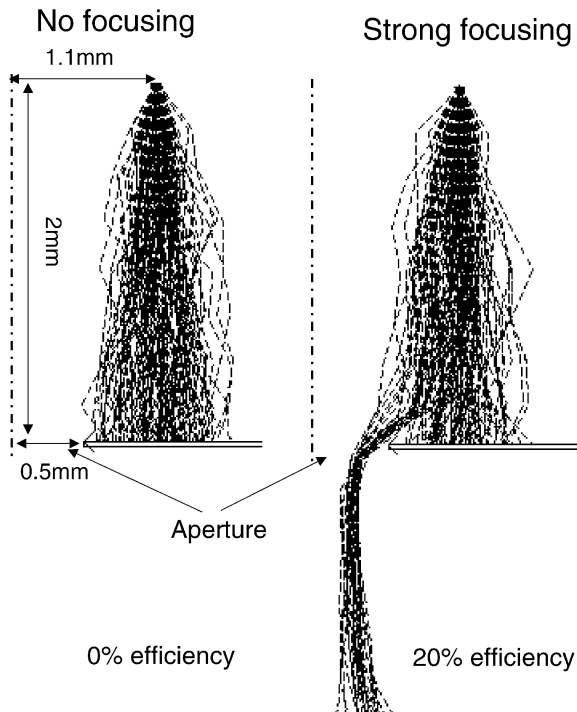


Fig. 3. Simulated single ion trajectories with and without focusing for ions deposited 2mm above the aperture and 1mm (two aperture radii) aside from the aperture axis (denoted by the dash-dot line).

kept at about 20 V/cm, which is below the gas multiplication threshold but sufficiently high to sweep away particle-induced electrons within one or two microseconds. Five microseconds after the beam particle trigger, the field  $E_1$  is raised to the desired value of 60 V/cm for 80  $\mu$ s, required for full ion clearing.

For detector calibration and monitoring of its long-term performance, we have incorporated an  $^{241}\text{Am}$  alpha source into the ND. We are using a gold-plated source, with an average energy of 4.25 MeV and a FWHM of 0.3 MeV; this corresponds to an average LET value of 107 keV/ $\mu$ m in water. A 1-mm diameter alpha particle beam of  $\sim 3$  particle/s is defined by a source collimator. The trigger is obtained by a PIN diode (Hamamatsu S1223-01), located behind the SV. The beam is crossing the SV orthogonal to its axis, at a distance of 15mm above the ion extraction aperture. The alpha-particle beam is in the same

plane but perpendicular to the accelerator beam (see above) and can be turned off using a shutter.

The operation of the IC necessitates a vacuum level close to  $10^{-5}$  Torr. The five-orders-of-magnitude pressure difference within our instrument is reached by a double-differential pumping system. It consists of two turbomolecular pumps (Varian VT250 and VT550, denoted Pump #1 and #2, respectively, in Fig. 1), a set of three orifices placed below the aperture, and a conical screen, deflecting the gas flow from the aperture and orifices into one of the pumps. To compensate for the continuous gas flow from the IV to the DV, gas is continuously added to the IV via a proportional regulating valve (MKS 248A). The pressure in the IV is controlled by a temperature-stabilized Baratron pressure gauge (MKS 128) and pressure control system (MKS 250E), with an accuracy of better than 0.01 Torr.

The three orifices placed below the ion extraction aperture serve as ion-focusing electrodes, generating the focusing field  $E_2$  near the aperture and focusing the extracted ions into the DV. The aperture and the focusing electrodes were gold-plated to avoid eventual distortions of the electric fields by up charging of oxidized surfaces. Their dimensions were selected to allow for maximal ion transmission, while keeping an efficient differential pumping. The respective diameters of the aperture and of the electrodes  $A_1$ – $A_4$  are 1, 3, 5, 5 and 4 mm; the distance between each two consecutive electrodes was 2.5 mm except for  $A_3$  and  $A_4$ , which were separated by 10 mm. The potentials on these electrodes as well as that in the IV were optimized for maximal ion transfer efficiency (see below).

Within the vacuum-operated DV, ions are accelerated onto the IC, which is a discrete dynode electron multiplier (SGE model AF180HIG), inducing secondary electron emission. The resulting electron multiplication permits efficient detection of individual ions and their counting. The IC is maintained at a potential difference (cathode to anode) of 2.5–3.5 kV, with the cathode kept at 8.2 kV above ground and the anode side connected to ground via a variable resistor. The ions, extracted from the IV, are therefore accelerated to 8.2 keV; this results in large signals well above noise and in high detection efficiencies [15]. To

avoid eventual discharges from the IC body to the vacuum chamber, the IC is surrounded by a helical copper shield, kept at the potential of the cathode. The signal is read out of the last dynode of the IC, decoupled from the high voltage via a pulse transformer. The signals are processed by a fast preamplifier, followed by a timing filter amplifier, resulting in 20 ns wide pulses, with amplitudes reaching up to 600 mV and with a noise level of 16 mV. Single ion pulses as well as a typical pulse trail from the IC are shown in Fig. 4.

## 2.2. Accelerator beam setup

The ion-counting nanodosimeter was mounted at the 14UD Pelletron accelerator at the Weizmann Institute of Science. Fig. 5 depicts the beam-line geometry: An ion beam crosses a thin scattering foil coupled to a 1 mm thick, 1 mm diameter circular tantalum collimator. The scattering foil induces a beam divergence of  $2\text{--}5^\circ$

(depending on the foil, particle and energy). A second, movable collimator of 1 mm diameter is located 1.74 m downstream from the scattering foil; it is used to adjust the pencil beam location within the SV. This arrangement results in a much reduced beam intensity without spoiling the energy distribution, see Table 1. The collimated ion beam enters the ND via a thin ( $2.5\ \mu\text{m}$ ) Mylar window of 15 mm diameter. Downstream of the ND and separated by a similar Mylar foil, we have placed a 2D-position sensitive multiwire proportional chamber (MWPC). The back of the MWPC is sealed with a 5 mm thick plastic scintillator, coupled to a photomultiplier tube (PMT); a 1 mm diameter collimator is placed in front of the scintillator.

The scattering foil thickness and the propane gas pressure in the MWPC were matched to the impinging ion type. For carbon ions, we used a  $25\ \mu\text{m}$  thick Mylar scattering foil and the MWPC was operated at 10 Torr; for protons, we used a  $200\ \mu\text{m}$  stainless steel scattering foil and the MWPC was operated at 90 Torr. The exact particle energies before and after the foil-degradation as well as their straggling (calculated using TRIM [16]) are given in Table 1.

Before each run, we have optically aligned the beam, with a precision of better than 0.2 mm, so that all measurements were performed with the *same beam geometry* and, therefore, were comparable. To ensure beam uniformity, we have scattered the primary beam to a diameter of  $>10\ \text{cm}$  and selected a small fraction with a 1 mm collimator. The resulting beam has a diameter of 1 mm with a divergence of about  $0.025^\circ$ ; it passes 15 mm above the center of the ion extraction aperture.

## 2.3. Trigger, DAQ system and analysis

The data acquisition (DAQ) system correlates between each projectile and its associated ions, registering the arrival time of each ion with respect to the trigger. Optionally, the DAQ records information regarding the projectile particle (energy, trajectory, etc.). In the offline analysis, the validity of each event is checked against strict

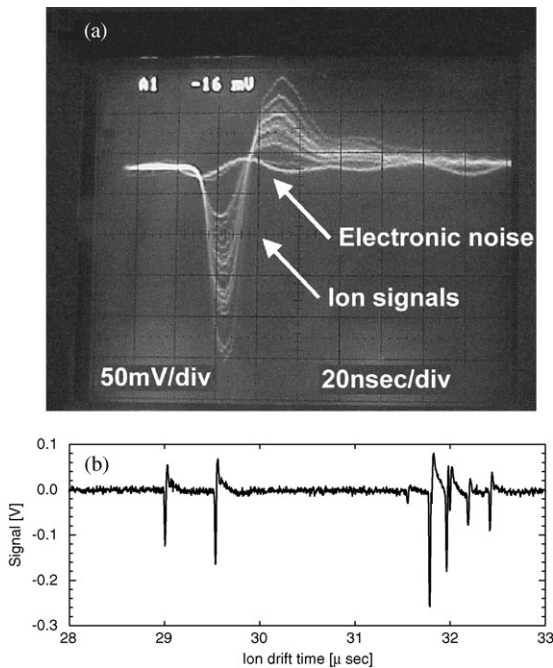


Fig. 4. Examples of single ion pulses recorded from the ion counter after a fast amplifier: (a) a photograph of single ion pulses taken off an oscilloscope, (b) ion pulse train of a single event induced by an alpha particle.

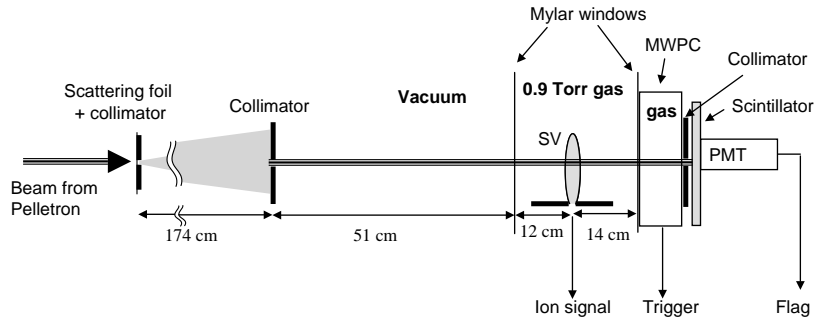


Fig. 5. A schematic diagram of the beam line layout. See text.

Table 1  
Measured average cluster sizes for various radiation fields

Projectile energy		LET (keV/ $\mu\text{m}$ )	Average cluster size (ions)
Before foil (MeV)	After foil (MeV)		
1. Protons			
22	$19.3 \pm 0.11$	2.3	0.29
17	$13.6 \pm 0.12$	3.6	0.38
12	$7.15 \pm 0.23$	6	0.63
2. Alpha particles			
	$4.25 \pm 0.27$	107	10.5
3. Carbon nuclei			
72	$62.8 \pm 0.13$	270	21.06
60	$49.2 \pm 0.13$	320	23.99
40	$24.8 \pm 0.15$	500	27.76

The energy degradation was calculated using Trim [16]. All measurements were done in the sensitive volume shown in Fig. 2b, in pulsed mode operation.

triggering requirements. Relevant events are selected and appropriate histograms are generated.

The event trigger is provided by the MWPC, which, ideally, detects all beam particles crossing the ND. We used a standard, 10-cm diameter MWPC (20  $\mu\text{m}$  anode wires, 1-mm pitch, 3.2-mm anode-to-cathode gap), preceded by a 3.2-mm thick parallel-grid pre-amplification gap. The MWPC anode provides the trigger signal to the ND DAQ system. The cathodes' wires are connected to delay-line readout circuit, providing an efficient means for 2D beam imaging. The

cathode signals are processed by fast amplifiers, two time-to-amplitude converters and a PC-borne ADC card (Ack2D) [17]. The MWPC permits visualizing the incident ion beam with sub-mm precision. This is useful during beam preparation and monitoring but is not included in the nanodosimeter DAQ.

Due to scattering of particles in the degradation foil, the ND windows and in the MWPC itself (the scattering in the gas is negligible), 80–95% of the particles detected by the MWPC do not provide a signal in the collimated scintillator, the exact amount depending on the beam type and energy. The DAQ system records all triggered events, and the selection on the collimated ones is done offline. This strategy is very important in order to ensure full elimination of pile-up ions from closely consecutive events, as will be discussed in Section 3.4.

The DAQ system is fed by negative fast analog pulses from the IC, the MWPC and the PMT. The pulses from the IC are properly shaped and recorded by a custom-designed, PC-based DAQ system shown schematically in Fig. 6. It is based on a National Instruments PCI6602 timer/counter card, essentially a PC-borne multi-channel 80-MHz time-to-digit converter. It is designed to digitize and record, in real-time, two data streams with a time resolution of about 25 ns (determined by the signal shaping hardware) and a rate up to 8 MB/s.

The trigger signal from the MWPC is injected into the “trigger” data stream of the PCI card. When working in pulsed mode of the electric field  $E_1$ , this signal is also used to activate, after a 5- $\mu\text{s}$

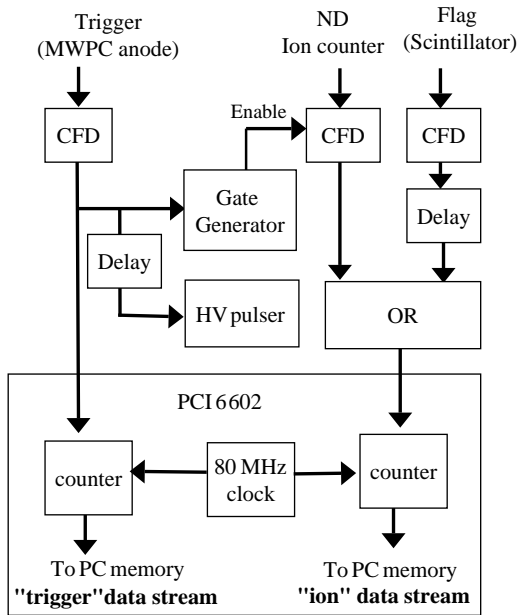


Fig. 6. A flow diagram of the DAQ system. See text for details.

delay, the high voltage ion-extraction pulse, and to generate an 80- $\mu$ s long gate signal for enabling the ion-counter channel discriminator. The “trigger” data stream is used by the DAQ as a time reference for measuring the ion arrival times and for offline pile-up rejection.

The “trigger” data stream can also be used to analyze the time structure of the primary beam, relevant in accelerators with pulsed beam structures, as is the case for experiments carried out at the Loma Linda proton accelerator.

The signals from the IC are injected, into the “ion” data stream of the PCI card. This provides information about the individual ion drift time and the number of ionizations per primary particle event.

The signal from the collimated scintillation detector is introduced as a logic flag for offline selection of collimated projectiles: it is delayed, and then incorporated into the “ion” data stream via an OR gate. The time delay is set such that this signal does not interfere with the ion pulses.

A data storage algorithm manages the data stream transfer to the PC computer hard disk. The full data analysis is carried out offline but a

simplified online data analysis is applied for rapid data diagnostics and control of proper system functioning.

The ion drift velocity in our experimental conditions is about 0.4 mm/ $\mu$ s, resulting in ion drift times of 20–40  $\mu$ s, depending on where the ion was created (see, for example, Fig. 7). This poses a limitation on the maximal possible beam rate; in order to avoid counting ions from two or more projectiles within the same cluster, we usually require a minimum interval of 80  $\mu$ s between consecutive projectiles.

In the offline analysis, we first performed the pile-up rejection, namely rejecting all events that are followed or preceded by another event within less than 80  $\mu$ s. We then selected those events marked by a logic flag. These events are attributed to projectiles belonging to a well-defined narrow beam in the ND.

Each dataset, typically of  $5 \times 10^5$  non-overlapping collimated events, was measured over a period of 2–3 hours, at beam rates of a few hundreds of particles/second. The analysis software then generated an ion cluster-size distribution, providing the frequency at which clusters of any given number of ions are induced by a single ionizing particle, within the SV. The analysis also provides the ion arrival time distribution; it is

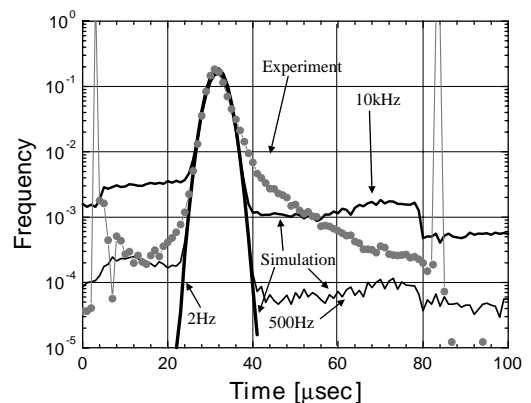


Fig. 7. Experimental and simulated ion arrival-time distributions at different particle rates. The Monte Carlo simulations were made under the same electric field conditions and for the same trigger efficiency as in the experiments. The two sharp spikes in the experimental data are due to pickup from the pulsed electric field.

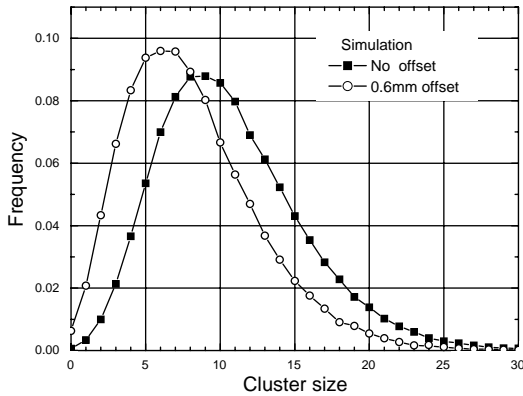


Fig. 8. Simulated alpha-particle induced cluster size distributions with the beam either centered on the sensitive volume or displaced by 0.6 mm (propane, 1 Torr).

correlated with the initial ion deposition location along the SV axis, namely its distance from the extraction aperture. This information may be used to measure the ionization density profile across the particle's track. It can also be used to sub-divide the data into selected time windows, equivalent to the division of the SV length into small segments, a few nanometers long. Due to the rather small ion diffusion in the gas (about 1 mm FWHM for 1 cm drift in our conditions), the information on the initial ion deposition distance is well preserved, with a resolution of a few nanometer in our conditions. This feature may serve as a basis for *experimental track-nanodosimetry*, providing a way of mapping ionization clusters deposited by a single projectile at different distances from the track axis.

#### 2.4. Monte Carlo simulations

A Monte Carlo simulation code was developed, based on experimental ionization cross-sections of protons, and on experimental electron interaction cross-sections for elastic scattering, excitation and ionization in propane (see Appendix A). The MC code takes into account the energy spread of the projectile beam, calculated with TRIM [16], and the simulated SV maps, to generate a prediction for the number of measured ions.

The MC simulation is an invaluable tool for the ND diagnostics. It enabled us to predict effects

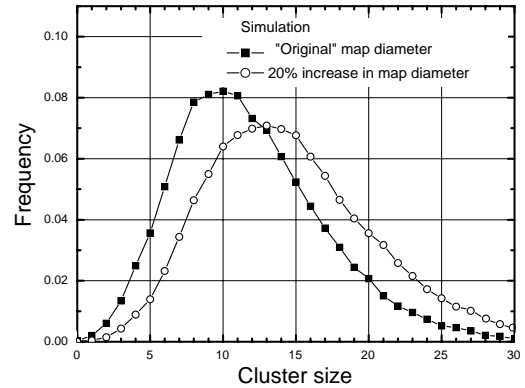


Fig. 9. Simulated alpha-particle induced cluster size distributions with SV maps varying in diameter by 20%. The average cluster size differs by 40% (propane, 1 Torr).

related to experimental parameters such as beam misalignment (Fig. 8), variations in beam size or in the SV (Fig. 9). Moreover, it enabled us to study effects that are inaccessible experimentally, such as separating the contributions from direct ionizations and from the  $\delta$ -electrons. The essential physical assumptions and cross-sections used in the MC are summarized in detail in the appendix.

### 3. Nanodosimeter performance

We have extensively studied the parameters affecting the nanodosimeter performance and its operation in an accelerator environment, trying to identify and minimize the systematic errors.

We have investigated: the effect of the IC response, ion focusing and ion cluster-size on the ion-counting efficiency; the effect of event repetition rate and trigger efficiency on pile-up rejection; the SV size and its sub-division by time selection; the role of beam geometry (alignment and diameter); the effect of secondary charge multiplication in the SV and their elimination by pulsing techniques. The results of these studies are presented below.

#### 3.1. Ion-counting efficiency

The number of ions induced in our nanometric SV ranges typically from zero or one for low LET

protons up to 100 for high LET carbon nuclei. Ion losses were seen due to inefficient transfer of the ions to the IC, inefficient ion detection in the IC and due to deficiency of the DAQ system. We have also seen an overcounting of ions due to pile-up events and charge multiplication in the IV and possibly also in the intermediate vacuum region.

### 3.1.1. The ion counter

As we are counting single ions, the efficiency of the IC to detect few-keV ions is of crucial importance. In a previous work [15], we reported on the absolute single-ion detection efficiency of our IC. It rises with the ion energy reaching an efficiency of about 90% for ions above 4 keV. Therefore, accelerating the ions in our setup to 8.2 keV ensures single ion detection efficiency values close to unity.

A special concern is the long-term degradation of the IC under vacuum of  $10^{-5}$  Torr of propane, which is not specified by the producer. We have conducted systematic aging studies, to assess the time evolution of the IC efficiency under continuous operation. These measurements were performed at pressures ranging from  $3 \times 10^{-6}$  to  $4 \times 10^{-5}$  Torr of argon, air, and propane, in conditions similar to those encountered during regular operation of the IC in our nanodosimeter.

It was found that the effect of the IC aging depends on the integral of its *output current*, regardless of the operating IC voltage. After accumulating 0.004 Coulombs (approximately  $10^8$  counted ions), the gain and the output pulse-height of a new IC typically dropped by about a factor of 2, regardless of the gas type and pressure. For all multipliers of this type, investigated within our application, it was found that the gain stabilizes at a minimal plateau value and does not continue to deteriorate. In some cases, we have seen a marked instantaneous drop in the efficiency, following exposure of the IC to an excessive ion flux (several nA) or to discharges. The dependence of the IC aging on the accumulated *output charge* indicates that the aging is connected to changes at the end of its dynode system while the input dynodes, which are essential for providing high ion-counting efficiency, are not seriously affected. In this case, the IC efficiency can be maintained at

its original value by increasing the IC operating voltage to recover the average pulse height and by corresponding adjustment of the electronic threshold. This was confirmed by direct measurements of the ion-counting efficiency of aged ICs. To make sure that all our measurements were performed under constant high efficiency, the pulse-height spectrum of the IC has been continuously monitored during experiments. Its ion-counting efficiency has been frequently verified by recording ion cluster distributions induced by alpha particles. No visible decrease in pulse height and therefore in efficiency was seen during the experiments described below, over a period of about a year.

### 3.1.2. Loss of ions due to DAQ dead time

The finite pulse duration combined with the communication protocol of the DAQ system result in a dead time of a few tens of nanoseconds following each ion. Therefore, if several ions, belonging to the same cluster, reach the IC within a few hundreds of nanoseconds, some of them could be missed. Moreover, it was found experimentally, that the counting deficiency, which affects the cluster size distribution, depends on the details of the ion arrival time distribution, as well as on the DAQ properties.

To study this, a series of MC simulations of the DAQ system were performed, using a Gaussian arrival-time distribution with an RMS value, taken from the experiment (Fig. 7). The distribution of time intervals (time between consecutive ions) for clusters of a given size, obtained from this simulation, with zero dead time, was compared with the experimental one (Fig. 10). The latter shows a deficiency at short time intervals with practically no measured intervals of less than 40 ns, corresponding to the width of the digital pulses entering the PCI card. In fact, the deficiency extends to time intervals longer than the electronics' dead time and was seen to depend on the cluster size. For example, for clusters of 40 ions, it extends to more than 200 ns, as seen in Fig. 10. This effect is believed to arise from data corruption within the PCI card or the PC data bus.

To evaluate the consequence of this undercounting on the cluster size distributions we

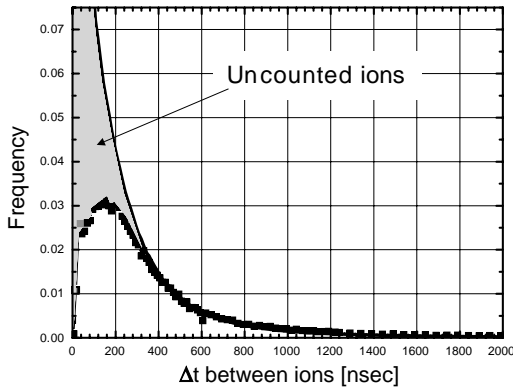


Fig. 10. Measured and simulated distributions of the time difference between consecutive ions in a 40-ion cluster. The solid line is the distribution expected from simulations. About 45% of the ions are missing from the experimental one.

introduced into the DAQ Monte Carlo simulation a cluster-size dependant *effective dead time*, namely a lower  $\Delta t$  cutoff in the curve of Fig. 10. As a result, for each cluster size, the area under the simulated and experimental curves is equal, thus approximating the experimentally observed undercounting. We then simulated the measured cluster sizes. Fig. 11 shows the results as function of the size  $n$  of the initial cluster deposited in the nanodosimeter. The dashed line represents the case without dead time. From this model study, we see that for small clusters up to about 5 ions, the undercounting amounts to  $<5\%$ . For clusters of 10 ions, the measured cluster size will be smaller than the real one by about 10%. For larger clusters the discrepancies are much larger.

This phenomenon limits the maximal cluster size that can be reliably measured with the current DAQ electronics. Fig. 12 shows the effect of the undercounting on *simulated* ion cluster size distributions induced by alpha particles and carbon nuclei. For the lower LET alpha particles, there is a small shift in the distribution peak of about 10%, but the whole distribution is somewhat distorted as the loss increases with cluster size. For the higher LET carbon nuclei, the situation is much worse as the average cluster size is more than 60 ions and half of them are lost due to the DAQ dead time.

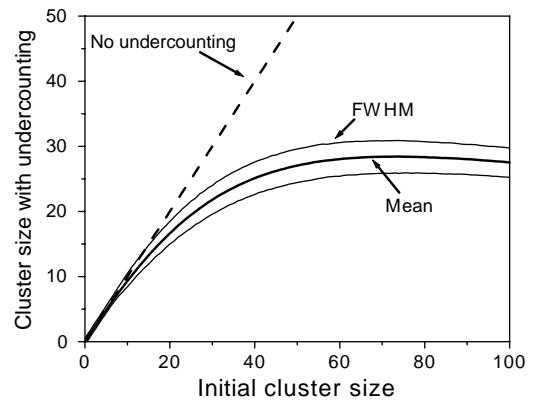


Fig. 11. The simulated effect of ion undercounting, due to cluster-size dependant dead time. Shown are the mean and FWHM values of the simulated cluster size distribution as function of the initially created cluster size, taking into account the DAQ parameters. The dashed line represents the ideal case without dead time.

### 3.1.3. Ion transfer to the IC

The ion transfer efficiency to the IC depends on the focusing field below the extraction aperture, which should be carefully optimized. This was done by monitoring the alpha-induced average ion cluster size variation with the voltages applied on the four electrodes below the aperture.

The first electrode ( $A_1$ ) controls most of the focusing field ( $E_2$ ) near the ion extraction aperture. The average cluster size increases linearly with the applied potential due to the focusing effect of  $E_2$ , leading to an increase in the SV diameter. Only at very high fields the relationship becomes non-linear due to secondary effects, possibly charge multiplication in the residual gas present in the intermediate vacuum region.

In addition, there is some electric field penetration from electrodes  $A_2$ – $A_4$  into the vicinity of the ion extraction aperture, which may affect the focusing field by as much as 10%, resulting in a slight increase of the SV. This increase of the field  $E_2$  was compensated by slightly decreasing the potential on the electrode  $A_1$ .

Significant losses of ions during their transport through the apertures  $A_1$ – $A_4$  were observed only in cases where the field below a given electrode was lower than that above it. The potential sequence

on the electrodes  $A_1$ – $A_4$  was optimized according to this criterion.

Based on these measurements we defined conditions for optimal transfer of ions from the ion extraction aperture to the IC. However, there is no practical way to prove that these “optimal” conditions indeed correspond to unity transfer efficiency. This point will be further discussed below.

### 3.2. The SV diameter and beam alignment

As expected, and verified by MC simulations, the ion cluster size distributions are rather sensitive to the actual size of the SV. Fig. 13 shows the *measured* ion cluster size distributions induced by 4.3 MeV alpha particles in the two sensitive volumes of Fig. 2. These two measurements differ

only in the value of  $E_2$ , the electric field below the ion extraction aperture. They demonstrate the flexibility of our ion counting nanodosimeter, which enables changing the SV diameter by modifying the applied potential on the electrode  $A_1$ . They also demonstrate the sensitivity of our ion counting nanodosimeter to the exact configuration of the SV. This is further established in Fig. 9, which shows *simulations* of alpha particle induced cluster size distributions; when the diameter of the SV is increased by 20% the peak shifts by 40%.

As the SV is rather small, of about 2 mm diameter in gas, and there is a strong variation in the ion collection efficiency across it, the beam alignment and shaping in a narrow beam irradiation mode, is of crucial importance. Fig. 8 illustrates this point, showing the effect of alignment on the *simulated* alpha-induced cluster size distributions. The mean cluster size drops by 40%

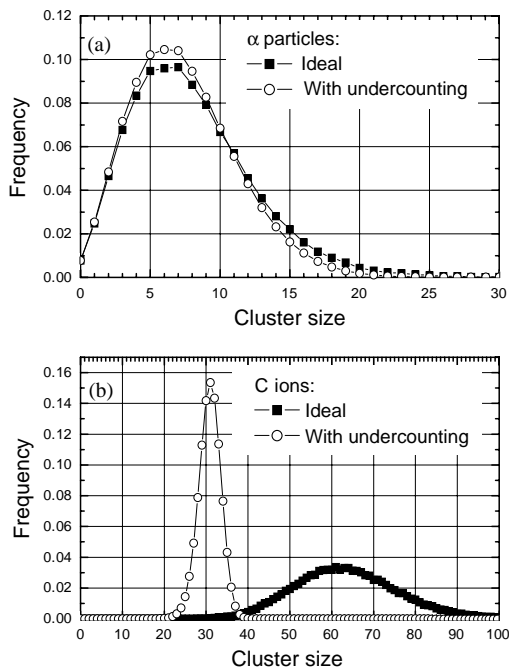


Fig. 12. The effect of undercounting on simulated cluster size distributions induced by 4.25 MeV alpha (a) and 24.8 MeV carbon (b) ions. The full and open symbols represent simulated cluster size distributions without and with model-calculated undercounting, respectively. For the alpha particles (LET = 107 keV/ $\mu$ m) the effect is mainly seen in the tail. For the carbon nuclei (LET =  $\sim$  500 keV/ $\mu$ m) the effect is very pronounced.

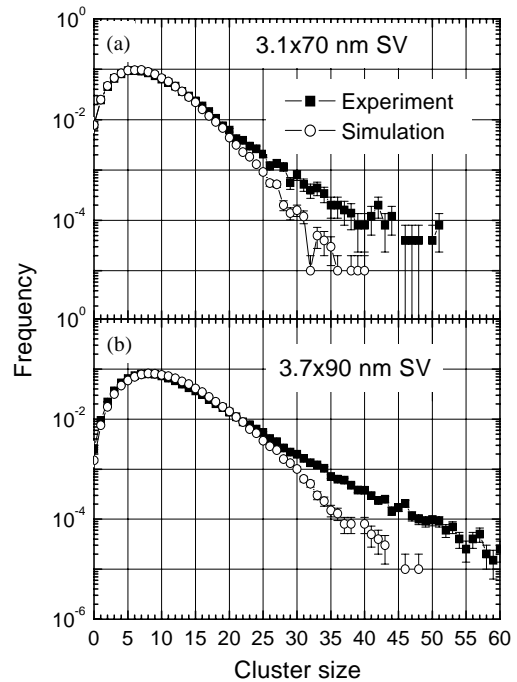


Fig. 13. Experimental (full symbols) and model simulated (empty symbols) cluster size distributions induced by 4.25 MeV alpha particles in the two respective (a, b) sensitive volumes depicted in Fig. 2 (propane, 0.9 Torr).

when the beam shifts from the center of the SV by 0.6 mm.

### 3.3. Charge multiplication within the SV

Fig. 14 shows the *measured* ion arrival time distributions induced by 4.3 MeV alpha particles, for cases where  $E_1$  is DC at 60 V/cm and when it is pulsed at 60 V/cm with an electron sweeping field of 20 V/cm. The origin of time was shifted by 5  $\mu$ s so that the peaks coincide. The spike at 60  $\mu$ s is due to pickup from the high voltage pulser. The excess of ions arriving after the main peak of the distribution in the DC mode is believed to be due to charge multiplication within the IV. Fig. 15 depicts the cluster size distribution from the same measurement, displaying a 10% increase in the mean number of ions in DC compared to pulsed mode. Our measured single electron gain in propane, as well as MC-calculated values of the Townsend coefficient, both predict an average gain of about 1.3 in the IV under the field of 60 V/cm. Considering the small ion extraction efficiency in the upper part of the SV, this is consistent with the measured 10% increase in the mean number of ions.

From systematic measurements of cluster size distributions induced by alpha particles in pulsed and DC modes, we have seen that the exact value of the sweeping field is not important as long as it

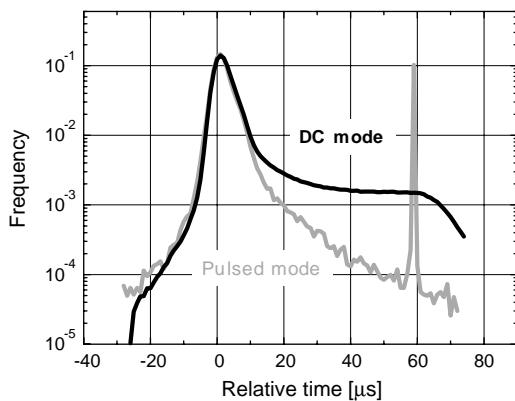


Fig. 14. Measured ion arrival time distributions in pulsed (60 V/cm pulse; 20 V/cm electron sweeping field) and DC (60 V/cm) modes. Note the large tail in DC mode, originating from the charge multiplication avalanche (propane, 0.9 Torr).

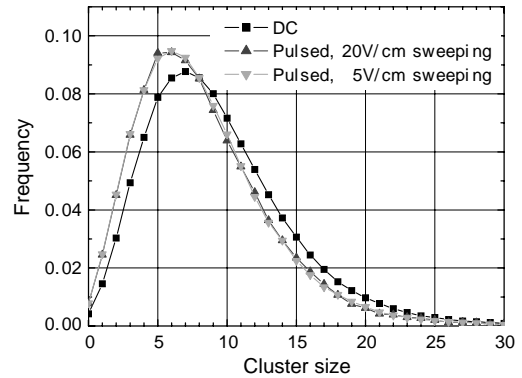


Fig. 15. Cluster size distributions induced by alpha particles in DC mode, and pulsed mode with low (5 V/cm) and high (20 V/cm) electron sweeping fields. The pulsed field and the DC fields are 60 V/cm (propane, 0.9 Torr).

is higher than a few V/cm required for electron clearing and lower than the onset of charge multiplication (roughly 40 V/cm). Nevertheless, it is important to choose the highest possible sweeping field, in order to minimize the interference of ions, induced by a no-trigger event, and thus having no high-voltage pulse. Such ions reside in the SV volume for very long times and may cause pile-up (see Section 3.4).

### 3.4. Trigger efficiency and pile-up rejection

At high event rates, where the average time between projectiles is comparable to the time required for ion clearing from the SV, there is a high probability that one or more additional projectiles will pass through the nanodosimeter before the ions of the previous projectile are extracted. For example, at 1 kHz this is expected for  $\sim 10\%$  of the projectiles. Unless such events are removed in the analysis, we will get a distorted cluster size distribution. The pile-up rejection described in Section 2.3 is based on the recorded time elapsed between two consecutive triggers, which relies on an efficient trigger. The MWPC pulses are indeed located well above noise, which should provide, a priori, an efficient trigger; however, we estimate that roughly 20% of the projectiles are scattered or absorbed in the first mesh of the MWPC, generating no signal and resulting in 80% trigger efficiency. (Replacing the

mesh by a thin metalized Mylar foil in future experiments is expected to raise the trigger efficiency close to unity.)

To evaluate the full consequence of the fact that our trigger does not have full efficiency, we have conducted MC simulation based on the *measured* ion arrival times and cluster size distributions, and on ion clearing times in pulsed mode. It shows that with a trigger efficiency of 80% and a beam flux of 10 kHz, more than 4% of all events will contain ions from consecutive non-triggering projectiles. At a beam flux of 500 particle/s, used in the experiments described here, the expected fraction of events with pile-up is  $\sim 0.2\%$ . The distortion expected by incomplete pile-up rejection to the cluster size distribution is shown in Fig. 16. We

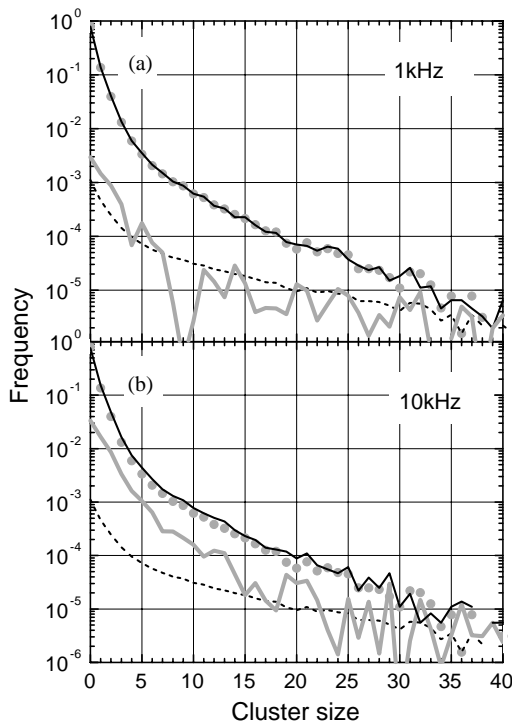


Fig. 16. The effect of pile-up on the measured proton-induced cluster size distributions. The dots are the measured distributions, used as an input to a MC simulation of the pile-ups (80% trigger efficiency, pulsed mode). The thin solid line is the resulting simulated cluster size distribution in the case of (a) 1 kHz counting rate and (b) 10 kHz counting rate. The absolute difference between the two distributions is shown as a thick line. The dotted line is the expected statistical error.

used a Gaussian fit to the ion arrival time distribution and a measured cluster size distribution as input and calculated the pile-up rejection with an inefficient trigger (efficiency of 80%) for trigger rates of 1 and 10 kHz, respectively. An input cluster size distribution (dots), results in distorted ones (thin line), due to inefficient pile-up rejection. The thick line depicts the pile-up component, which is statistically significant only for event rates above 1 kHz.

We have seen from simulations and measurements alike that trigger inefficiency also influences the ion arrival time distribution, as shown in Fig. 7. This figure compares ion arrival time distributions *simulated* for rates of 2 Hz, 500 Hz, and 10 kHz, with a trigger efficiency of 80%. A typical *measured* ion arrival time distribution, taken at a beam flux of  $\sim 600$  Hz is shown for reference. Under conditions where the trigger is inefficient and the rate is high, we see a uniform pedestal in the time distribution. This pedestal represents the arrival time of ions not correlated with the trigger, namely ions from non-triggering projectiles. We see that for the lowest rate there are no pile-up ions; at 500 Hz there are roughly 1% of pile-up-induced ions, which are distributed randomly between 0.2% of the events, resulting in unnoticeable distortion of the cluster size distribution (e.g. Fig. 16a, the distortion is still unnoticeable). At 10 kHz, however, roughly 10% of additional ions are induced by pile-up and distributed between 4% of the events, resulting in a statistically significant distortion. We used this feature in the ion arrival time spectrum in order to adjust the beam rate during the experiments, maintaining the pedestal level such that less than 1% of the measured ions are due to non-triggering projectiles.

The excess of ions in the measured distribution, at times longer than  $40 \mu\text{s}$ , corresponds to a 10% deviation from the expected Gaussian arrival time distribution, and is currently under investigation.

### 3.5. Measurements in segments of the SV

The SV used in our experiments, Fig. 2b, may be too large for some applications. We recall that in modeling DNA damage, for example, the length of

the relevant segment is  $\sim 16$  nm. However, with the present technique we are recording the arrival time of each ion; it is therefore possible to *select offline* ions deposited within a certain time-window, along the symmetry axis of the SV, namely at a given distance from the aperture and within a determined SV length. This allows us to obtain sensitive volumes of different length corresponding to targets of different length in condensed matter. The segments of our large SV can be determined along its axis with a resolution of  $\sim 2$  nm, as defined by the diffusion of ions in the IV gas.

Fig. 17 demonstrates the segmented SV technique and is based on the data presented in Ref. [13]. These data were measured in DC mode (see Section 3.3) and are given as a demonstration of the segmenting principle. Fig. 17a shows *measured* cluster size distributions induced by 13.6 MeV protons in segments of the SV, centered on the

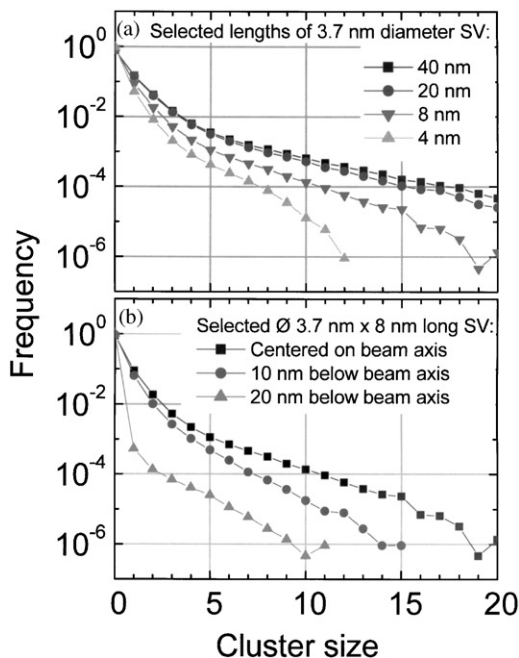


Fig. 17. Experimental results of ionization cluster-size distributions, induced in selected slices along the axis of the sensitive volume shown in Fig. 2b. These distributions were derived from data presented elsewhere [13], selecting various ion arrival time windows, and are shown here to demonstrate the technique.

$\sim 2$  nm diameter pencil beam, extending over 4, 8, 20 and 40 nm length. The 20 nm long SV fraction corresponds roughly to the required SV for modeling DNA damage.

Fig. 17b shows the *measured* cluster size distributions within segments of the SV, 3.7 nm diameter and 8 nm long, placed at different distances from the beam axis: centered on the beam axis, and displaced towards the aperture plane by 10 and 20 nm. Such an analysis, namely a “scanning” of the SV by time-window selection of the data, could be useful for studies of the ionization profile of a particle track.

#### 4. Cluster size distributions

We have measured nanodosimetric cluster size distributions, induced by protons, alpha particles and carbon nuclei of different LET values. The results are summarized in Table 1 and in Figs. 13 and 18. The measurements were done at relatively low particle rates (0.1–1 kHz), in pulsed mode, using narrow particle beams as described in Section 2.2.

The radiation fields were selected such as to span a large range of LET values. Protons of 7–20 MeV have LET values in water between 2.7 and 6 keV/ $\mu$ m. At such low LET values large clusters are rather rare and 50–90% of the projectiles generate no ions within the SV. As expected, the average cluster size (Table 1) rises linearly with LET, by approximately one ion for every 10.5 keV/ $\mu$ m, up to LET values of  $\sim 100$  keV/ $\mu$ m, where ion undercounting begins to distort the measurements—see Section 3.1.2. Fig. 18a–c also shows a comparison between the *measured* and *MC-calculated* cluster size distributions for protons. There is a very good correspondence between the measurements and simulations, down to frequencies of about  $2 \times 10^{-3}$  ( $\sim 6$  ions per cluster). For larger clusters, we have an excess of measured ions with respect to the simulation; it will be discussed below.

Cluster size distributions induced by higher LET radiation fields, namely alpha particles and carbon nuclei were measured in the LET range of 100 to  $> 500$  keV/ $\mu$ m in water (see Figs. 13 and 18d–f). At

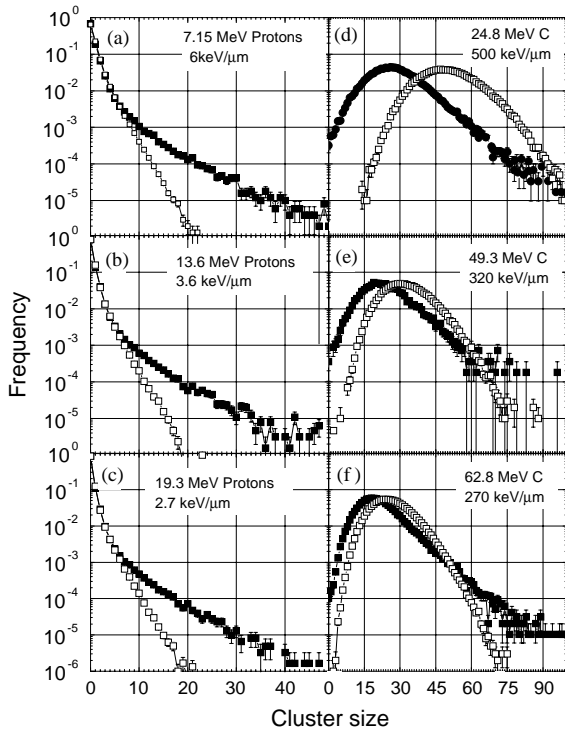


Fig. 18. Experimental (full symbols) and simulated (open symbols) ionization cluster-size distributions for protons and carbon ions of different energies.

such high LET values, the measured average cluster size is between 10 and  $>30$  ions and undercounting of ions (described above) becomes evident. Consequently, the correspondence between the measurements and the simulations becomes worse with rising LET. In the alpha particle data (Fig. 13b) the undercounting only leads to a small shift in the peak of the distribution of about 10%, whereas in the carbon data (Fig. 18d–f) it is clearly manifested as a large shift of the whole distribution.

As with the proton data, here too there is an excess of large clusters compared to that expected from the MC. This is clearly seen as an excess of clusters larger than  $\sim 20$  ions in the alpha particle data (Fig. 13). In the carbon data (Fig. 18d–f), the excess is seen as a change in the slope of the cluster size distribution, as compared to that of the MC.

## 5. Discussion and summary

The ion counting nanodosimeter aims at precisely measuring, event by event, the number of ions generated within a gas volume, modeling a nanometric volume of condensed matter, immersed in a radiation field. The principle motivation for this are studies of radiation damage to biological targets such as the DNA molecule; however, by using appropriate gases and SV sizes, other condensed matter targets, such as sub-micron electronics, can be modeled.

We have measured particle-induced ion cluster size distributions in the LET range of 2.7 to  $>500$  keV/ $\mu\text{m}$  (in water); these measurements were performed using a collimated internal alpha source as well as narrow beams of low-energy protons and carbon nuclei at the Pelletron accelerator of the Weizmann Institute of Science. Similar measurements are currently being carried out at the Loma Linda University-Medical Center's Proton Synchrotron, measuring cluster size distributions induced by 40–250 MeV protons, in the LET range of 0.4–1.5 keV/ $\mu\text{m}$ , corresponding to the values typically encountered in radiation therapy or in space.

We have seen that, as expected, the average cluster size increases approximately linearly with LET up to  $\sim 100$  keV/ $\mu\text{m}$  (Fig. 19). However, it should be stressed that the *strength* of the nanodosimetric technique is that it provides us not only with average values of deposited ionization, but also with the full probability distribution of ionization clusters of a given size occurring within the defined SV. This permits detecting rare highly ionizing events, which may be associated with severely clustered damages to the target at the nanometer level. Neither the average cluster size nor the LET are sensitive to the occurrence of these large clusters, since their frequency is extremely small.

In parallel to the experimental work, we have developed a dedicated Monte Carlo code that simulates the most important phenomena related to the deposition of energy within the nanodosimeter gas and the ion detection process (see appendix). It was found to be an important tool for the development of the nanodosimeter and for

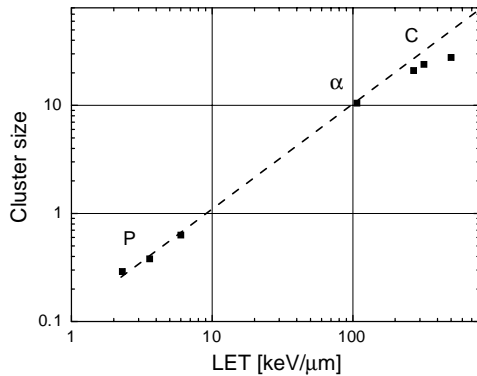


Fig. 19. Dependence of the measured average cluster size in 0.9 Torr of propane, with different projectiles, on the LET (in water). The dashed line is given to guide the eye. The deviation from linearity at large LET values is due to ion-pulse undercounting as described in Section 3.1.2.

the understanding of the measured results. The details of the physical processes and parameters included in the code are provided in the appendix to this work.

We have compared the measured cluster size distributions induced by protons and alpha particles to Monte Carlo simulations and have seen a rather good correspondence down to ion cluster frequencies of about  $10^{-3}$ ; at lower frequencies, the experimental data show an excess of large ion-clusters, compared to the simulation results. This was seen with all projectiles (see Section 4).

Three mechanisms were suggested that could lead to such an *overcounting* of ions, namely charge multiplication, event pile-up and K-shell ionization. The possibility that this excess is caused by beam contamination has been ruled out by recent experiments, using a spectroscopic solid state detector as trigger and performing offline selection of events having a well defined proton energy.

Charge multiplication was seen to take place when  $E_1$  exceeded 40 V/cm. This was overcome by pulsing the field  $E_1$  (see Section 3.3).

Overcounting due to event pile-up was observed at high beam rates, when two or more projectiles may traverse the SV within the time interval of ion

collection. The majority of pile-up events are eliminated by the offline analysis. With the current trigger efficiency (80%) and at a beam flux of 500 Hz, roughly 0.2% of the events remain that are affected by pile-up and the total number of counted ions is falsely increased by about 1%. However, we have seen from simulations (Fig. 16) that this does not result in any statistically significant distortion of the cluster size distribution induced by protons. For alpha particles the rate is too low to produce pile-up. As for the carbon nuclei, the undercounting induced by the DAQ system will mask such a small increase in the counted number of ions.

It has also been suggested that ion excess may be due to the (rare) ejection of a K-shell electron in one of the carbon atoms of propane. This process was not taken into account in our original MC code (and is not present in the simulations shown above), and may result in large clusters, as a 270 eV Auger electron is released in addition to the K-electron. However, this effect, which was recently added to the MC simulation, only accounts for about  $\frac{1}{3}$  of the observed effect.

None of the above mechanisms, though contributing to the systematic errors and data distortions, can explain the discrepancy seen between the measurements and the simulations for protons and alpha particles at rare clusters of frequency below  $10^{-3}$ . It appears that we encounter an unknown rare process ( $\sim 10^{-3}$  of all events) resulting in very large ion clusters.

We are currently investigating the possibility that the ion excess originates from rare ionizations occurring within the nanodosimeter, in the intermediate vacuum region. Such ionizations may form additional electrons, capable of initiating secondary avalanches in the dilute gas, under very high reduced-electric-field values; these would generate copious additional ions.

On the other hand, several mechanisms exist that could cause a *reduction* in the number of counted ions:

One such mechanism could originate from inefficient transport and detection of ions within the nanodosimeter. Our studies of the detection efficiency of the ion counter (IC) indicate that those ions reaching the counter are detected with

about unit efficiency. Although we cannot directly measure the transfer efficiency of ions from the SV to the IC, its dependence on the electrode voltages indicates that it is certainly above 90%.

A second mechanism is the dead-time of the DAQ system. It results in an underestimation of the frequency of large clusters (of more than 20 ions). This undercounting may be overcome by the use of a faster DAQ system, and in particular by an increase of the communication rate with the PC. Another possible solution is to use a slower gas or one with higher diffusion, as a target. In such a case, the average time interval between ions will be larger and the dead-time will have a smaller effect on the measured cluster size. This solution will, of course, strongly reduce the acceptable particle event rate and impose more stringent limitations on the trigger detector efficiency. Under the current conditions, this undercounting mechanism limits the applicability of our nanodosimeter to LETs below  $\sim 100$  keV/ $\mu\text{m}$ , where the average cluster size is  $\sim 10$ .

Regarding the application of DNA radiation damage, it should be noted that the number of biomolecules that can be damaged within a short segment of DNA is limited, and for high LETs several ionizations may occur on the same molecule. For example, calculations [18] indicate that the efficiency of double strand break production per molecular damage *decreases* if the number of individual damages is 10 or larger. In such case the measured cluster size distributions could still be relevant, even for high LET radiation.

An important source of systematic error studied in this work relates to the size and shape of the SV and to the beam alignment. The significance of these systematic errors is in our interpretation of the measured cluster size. To minimize the errors we have carefully verified the ND alignment before each experiment, with an accuracy of better than 0.2 mm; based on simulations, a 0.2 mm misalignment is expected to *reduce* the average cluster size by less than 3%.

Our understanding of the SV shape is based on MC simulations of ion transport within a calculated electric field distribution. The rather good correspondence between the simulation and measurements regarding the mean cluster size, for

several sensitive volumes, indicates that there is no gross error in our evaluation of the SV, particularly in view of the sensitivity of the average cluster size to the SV size, as shown in Section 3.2.

However, these observations only indicate an overall consistency and cannot replace a direct measurement of the SV. Using a narrow particle probe, it is, in principle, possible to experimentally measure the width of the SV; however, due to the long range of  $\delta$ -electrons produced by the available radiation fields, such a probe actually does not exist. We are currently developing mathematical methods for extracting the SV size from an experiment performed using a monoenergetic proton beam (which is not narrow), as will be described in a separate work.

The presented data demonstrate the strength and the limitations of ion-counting nanodosimetry. Compared to other nanodosimetric techniques, discussed in the introduction, the ion-counting nanodosimeter has a true *wall-less SV*, with the capability of sub-dividing it into small sub-sections for ionization-correlation measurements; such sub-division can be made either online, with simple time-gating electronics, or offline, during data analysis. The present ion-counting nanodosimeter can operate, in principle, at moderate particle repetition rates (up to 10kHz—using a fully efficient trigger), with practically any type of gas; the latter permits simulating other condensed media than tissue, e.g. with relevance to micro- and nanoelectronics. Our technique permits evaluating the absolute frequency of very large and rare clusters, down to levels below  $10^{-3}$ , with reasonable accuracy, running few-hour long experiments.

One should be reminded that the results presented in this work were measured with narrow particle beams, of a diameter smaller than that of the SV, for the purpose of instrument's characterization; therefore, the present data have no significance for radiation damage interpretation. In radiobiological experiments, one usually has no control over the trajectory of the particles in relation to the DNA molecule. Therefore, nanodosimetric experiments simulating the irradiation of DNA have to be carried out with broad particle beams, having diameters much larger than that of

the sensitive volume. Such experiments are in course.

Nanodosimetric experiments with broad particle beams will eventually be correlated with DNA-irradiation experiments to provide parameters for biophysical models that predict the yields of clustered DNA damages produced by multiple ionizations and their reactive intermediates at the nanometer level [19]. Such models are expected to pave ways to a better understanding and characterizing radiation damage to the living cell.

### Acknowledgements

The authors are indebted to Prof. M. Hass, Dr. O. Heber, G.P. Guedes, Y. Shrot and especially to Y. Shachar for their assistance with the accelerator experiments and to M. Klin for his technical assistance. S. Shchemelinin is supported by the state of Israel, the Ministry of Absorption and the Center for Absorption of Scientists. A. Breskin is the W. P. Reuther Professor of Research in the peaceful uses of Atomic Energy.

This work was partially supported by the National Medical Technology Testbed Inc. (NMTB) under the US Department of the Army Medical Research Acquisition Activity, Cooperative Agreement Number DAMD17-97-2-7016 and by the MINERVA Foundation. The views, opinions and/or findings contained in this report are those of the authors and should not be construed as a position, policy, decision or endorsement of the US Federal Government and NMTB.

### Appendix A. Simulation of track structure of protons, alpha particles and carbon ions

The MC model developed for simulating the formation of ionization clusters in the ND is based on the following assumptions, valid for ions at energies above 1 MeV/amu:

1. The initial particle energy is not significantly changed by inelastic interactions of the primary particles, while penetrating through the IV of the ND.

2. The energy and the flight direction of the particles within the ND are also not markedly changed by elastic interactions.
3. Electron capture or electron stripping processes along the particles' path within the ND do not influence ionization-cluster formation.

The first of these assumptions is justified, for instance, by the electronic stopping power of the particles, which is equal to  $316.3 \text{ eV cm}^2/\mu\text{g}$  and  $1253 \text{ eV cm}^2/\mu\text{g}$  for 1 MeV protons and 4 MeV alpha particles in propane, respectively [20]. These stopping powers lead to an energy loss of about 0.7% if a penetration length of 10 cm through propane at 0.9 Torr and 25°C (density  $2.1 \mu\text{g/cm}^3$ ) is assumed. The corresponding energy loss of 12 MeV bare carbon ions is about 2%. The validity of the second assumption is obvious both from the nuclear stopping power, which is much smaller than the electronic stopping power at higher particle energies, and from the particles' detour factor. For 1 MeV protons and 4 MeV alpha particles, for instance, the detour factors in propane [20] are 0.9949 and 0.9959, respectively, thus demonstrating that the particles' projected ranges are almost equal to their continuous-slowing-down ranges. The third assumption can be justified based on the results of Baek and Grosswendt [21] with respect to the influence of charge changing processes of protons on their  $W$  value.

The main steps for simulating the ionization pattern of track segments of light ions in propane are, therefore:

1. Determination of the distance to the subsequent point of ionization impact interaction.
2. Determination of the energy and direction of secondary electrons ejected by ionization processes.
3. Simulation of the slowing-down of these electrons in propane.
4. Analysis of ionization-cluster formation taking into account the efficiency map, which defines the sensitive volume of the ND.

#### A.1. Ionization patterns produced by the ions

According to the basic assumptions made in our MC model, the distance an ion has to travel

between two subsequent interaction points is governed by an exponential probability density which is characterized by the particle's mean free path length with respect to ionization. This mean free path length is equal to  $[N\sigma_{\text{ion}}(T_v)]^{-1}$  where  $N$  is the number density of target molecules, and  $\sigma_{\text{ion}}(T_v)$  the integral ionization cross-section of particles of type  $v$  at energy  $T_v$ . The integrated ionization cross-section is, therefore, the key quantity of ion cluster formation.

*Protons:* In the present MC model,  $\sigma_{\text{ion}}(T_v)$  for protons is calculated using the analytical functions and experimentally based parameters of Rudd et al. [22]. Since the appropriate parameters for propane are missing, those for methane are applied after scaling by the ratio of the number of weakly bound electrons of both molecules, as proposed by Wilson and Toburen [23]. To simulate the secondary electron distribution after proton impact ionization, we used the single-differential cross-sections of the Hansen-Kocbach-Stolterfoht (HKS) model [24] with respect to the secondary-electron energy for specific sub-shell  $v$  with binding energy  $B_v$  and electron occupation number  $N_v$ . The values of  $B_v$  and  $N_v$  are taken from Hwang et al. [25] for 10 orbitals of outer or weakly bound valence electrons of propane. The advantage of using the semi-empirical HKS model is that it has no adjustable parameters and it gives the single-differential as well as the double-differential cross-sections with respect to the energy and the emission angle of the secondary electrons. The model is also applicable to particles other than protons.

After selecting the secondary electron energy, the polar angle  $\theta$  of the electron's trajectory relative to that of the proton is sampled. For that we use the double-differential cross-section of the HKS model at specific electron energy, normalized to its integral over  $\cos(\theta)$  within the limits  $-1 \leq \cos(\theta) \leq 1$ . The azimuthal angle of the electron direction is assumed to be uniformly distributed between 0 and  $2\pi$ . These data are then used as input parameters to the Monte Carlo model for electrons, which is shortly described in Section A.2.

*Alpha particles and carbon ions:* As no experimental integral ionization cross-sections of alpha

particles or carbon ions at specified energy  $T_v$  are available in the energy range of our measurements, we use the experimentally based cross-sections for protons at energy  $T_p = (m_p/m_v)T_v$ , where  $m_p$  represents the proton mass and  $m_v$  the mass of alpha particles or carbon nuclei. To take into account the dependence of the ionization cross-section on the charge of the projectile, the proton cross-sections are multiplied by a scaling factor, proportional to the square of the projectiles' atomic number  $Z_v$ , according to first order Born approximation to the Bethe theory. A deviation from the  $Z^2$ -dependence is included, based on the ratio of the ionization cross-section for alpha particles or bare carbon nuclei in He to the cross-section of protons in He at the same velocity, multiplied by  $Z_v^2$  (as given in figure 4.16 of Report 55 of ICRU [24]). This leads to a reduction of the ionization cross-section, for instance, by 3.6% in the case of 4 MeV alpha particles and by 18.4% for 12 MeV bare carbon ions. To take into account the charge state of the particles on their way through our ND, a charge state equilibrium is assumed and the ratio  $Z_{\text{eff}}^2/Z_v^2$  is used as a further correction to the ionization cross-section for particle  $v$ . Based on the procedure of Ziegler and Manoyan [26] to determine  $Z_{\text{eff}}^2$ , this correction leads to a further reduction of the ionization cross-section by about 6% for 4 MeV alpha particles and by 31.1% for 12 MeV carbon ions. Both types of corrections become smaller with increasing particle energy.

## A.2. Ionization patterns produced by the secondary electrons

The histories of all electrons produced in propane are followed from one interaction point to the other, taking into account elastic electron scattering, different excitation interactions, and impact ionization. The main steps for simulating the propagation of electrons through propane are, therefore:

1. Determination of the distance to the subsequent point of interaction.
2. Determination of the type of interaction the electron will suffer at this point.

### 3. Sampling of the energy loss and flight direction resulting from the interaction selected in step 2.

As external electromagnetic fields are not included, it is assumed that the electrons travel along straight lines connecting subsequent interaction points. To determine the traveling distance, we assume that the target molecules can be treated as independent points homogeneously distributed in space. In this case the traveling distance is governed by an exponential probability density, which is characterized by the mean free interaction length of the electrons. This mean free interaction length is equal to  $[N\sigma_{\text{tot}}(T)]^{-1}$ , where  $N$  is the number density of target molecules, and  $\sigma_{\text{tot}}(T)$  the total scattering cross-section at electron energy  $T$ :

$$\sigma_{\text{tot}}(T) = \sigma_{\text{el}}(T) + \sum_j \sigma_{\text{exc}}^{(j)}(T) + \sigma_{\text{ion}}(T). \quad (\text{A.1})$$

Here,  $\sigma_{\text{el}}(T)$  is the elastic scattering cross-section,  $\sigma_{\text{exc}}^{(j)}(T)$  the cross-section for the excitation of a propane molecule to a state  $j$ , and  $\sigma_{\text{ion}}(T)$  is the total ionization cross-section.

The type of interaction that the electron suffers at each interaction point is sampled from the set of discrete probabilities,  $p_v(T)$ . These interaction probabilities are equal to the ratio of the cross-section of a given interaction process  $\sigma_v(T)$  to the total electron scattering,  $\sigma_{\text{tot}}(T)$ .

In the case of elastic interaction, the polar angle of the electron's flight direction after scattering relative to its initial direction is determined on the basis of the differential elastic cross-section. We assume that the azimuthal scattering angle is uniformly distributed between 0 and  $2\pi$ . If an excitation to a particular state  $j$  has been selected, the initial electron energy is reduced by the excitation energy required for the process but the electron direction is assumed to remain unchanged. In the case of impact ionization (only single ionization is taken into account), a secondary electron is ejected, which may contribute to the ionization pattern and must, therefore, be followed in the same manner as the primary electron.

The complete history of any electron is simulated until it leaves the volume of interest or until its energy becomes smaller than 10 eV, below

the lowest ionization threshold of 11.08 eV in propane.

#### A.2.1. Electron scattering cross-sections in propane

The cross-sections used for the present simulation in propane are based mostly on experimental data; they are described by analytical functions, useful for extrapolation and interpolation purposes. For the details of the evaluation of cross-sections and of their test, see the publication of De Nardo et al. [27].

(i) *Elastic electron scattering*: The treatment of elastic electron scattering was based on Rutherford's differential cross-section  $(d\sigma/d\Omega)_{\text{el}}$  with respect to the solid angle, modified to take into account atomic screening effects:

$$\left(\frac{d\sigma(T)}{d\Omega}\right)_{\text{el}} = \frac{Z(Z+1)e^4}{(1 - \cos\vartheta + 2\eta)^2(4\pi\epsilon_0)^2} \times \left[\frac{T + mc^2}{T(T + 2mc^2)}\right]^2. \quad (\text{A.2})$$

Here  $\vartheta$  is the polar angle of scattering relative to the initial electron direction,  $T$  the kinetic electron energy,  $Z$  is the atomic number of the target atom,  $e$  the electron charge,  $\epsilon_0$  the permittivity of vacuum,  $mc^2$  the electron rest energy, and  $\eta$  is the so-called screening parameter.

The integral elastic electron scattering cross-section  $\sigma_{\text{el}}(T)$  at kinetic energy  $T$  is obtained by integration of Eq. (A.2) with respect to the solid angle:

$$\sigma_{\text{el}}(T) = \frac{Z(Z+1)\pi e^4}{\eta(1+\eta)(4\pi\epsilon_0)^2} \left[\frac{T + mc^2}{T(T + 2mc^2)}\right]^2. \quad (\text{A.3})$$

The last equation was used to determine the screening parameter  $\eta$  as function of electron energy  $T$ , on the basis of integral cross-sections,  $\sigma_{\text{el}}(T)$ , derived from experiments, as proposed by Grosswendt and Waibel [28]. The polar angle of scattering is then sampled conventionally using the differential elastic cross-section. This procedure is a satisfactory approximation of differential elastic scattering at energies greater than about 200 eV, at smaller energies, however, large angle scattering is strongly underestimated. Because of this, a correction factor is applied at lower electron energies.

(ii) *Impact ionization*: The ionization part of our Monte Carlo simulation of electron histories is based almost exclusively on the integral ionization cross-section  $\sigma_{\text{ion}}(T)$  used by Chouki [29] in his analysis of swarm data, somewhat modified to get a better agreement with direct cross-section measurements near the ionization threshold.  $\sigma_{\text{ion}}(T)$  can be described by the following analytical function, which is consistent with the Bethe theory:

$$\begin{aligned} \sigma_{\text{ion}}(T) = & 4\pi a_0^2 \frac{c_1}{(T/R)} \ln \left( 1 + \frac{T-I}{R} \right) \\ & \times [e^{-c_2/(T/R)} + c_3 e^{-c_4/(T/R)} \\ & + c_5 e^{-(T-I)c_6/R(T/R)^2}]. \end{aligned} \quad (\text{A.4})$$

Here  $a_0$  is the Bohr radius,  $R = 13.61$  eV is the Rydberg constant,  $I = 11.08$  eV is the lowest ionization threshold of propane, and  $c_v$ ,  $v = 1, 2, \dots, 6$  are dimensionless fitting parameters [27].

The energy distribution of secondary electrons emitted after electron impact ionization was determined from a single-differential cross-section  $d\sigma(T)/d\varepsilon$  (where  $\varepsilon$  is the outgoing electron's kinetic energy) expressed by the Breit-Wigner formula, as proposed by Green and Sawada [30]. As the parameters describing  $d\sigma(T)/d\varepsilon$  in propane are not included in the tables of Green and Sawada [30] we use the data for methane. The errors induced by this procedure, due to the wrong shape of the energy distribution, for slow electrons in particular, and the non-ideal behavior at high energies, is acceptable for most applications.

The energy  $T'$  of the primary electron after impact ionization is calculated according to  $T' = [T - \varepsilon - I(T)]$ , where  $I(T)$  is the ionization threshold energy applied at a specified electron energy  $T$ . This ionization threshold is assumed to depend on the electron energy  $T$ , to approximate the contribution of sub-shells with binding energies greater than the lowest ionization threshold of 11.08 eV, which can contribute to  $\sigma_{\text{ion}}$  if the electron energy is high enough.  $I(T)$  was set equal to the average binding energy of the weakly bound valence electrons of propane, calculated on the basis of the partial electron ionization cross-sections of Hwang et al. [25].

No appropriate experimental data exist for the flight directions of the electron after scattering and of the ejected secondary electron. Therefore, the flight directions were determined approximately, using the kinematic equations proposed by Berger [31], which are based on momentum and energy conservation. The azimuthal angles of the electron after scattering and the secondary electron are assumed to differ by  $\pi$  and one of the two angles is assumed uniformly distributed between 0 and  $2\pi$ . This procedure represents a satisfactory approximation of the measured data of Opal et al. [32], at energies above  $\sim 200$  eV. At lower energies the following assumptions [28] are made, which are more consistent with the experimental data:

1. Secondary electrons at energies smaller than 50 eV are emitted isotropically.
2. In the energy range between 50 and 200 eV, 90% of the secondary electrons are emitted in the angular range between  $45^\circ$  and  $90^\circ$  whereas the rest are emitted isotropically.
3. The scattering angle of primary electrons, at energies above 100 eV after an ionization event, is given by Berger's equation. It is uniformly distributed between  $0^\circ$  and  $45^\circ$  at smaller energies.

(iii) *Impact excitation*: The treatment of excitation processes in propane was also largely based on the data set of Chouki [29]. It contains one discrete excitation cross-section with a threshold at 9.13 eV, a series of cross-sections for vibrational excitation, one cross-section for molecular dissociation and one for electron attachment.

The discrete excitation cross-section was fitted to an empirical function similar to that used for impact ionization:

$$\begin{aligned} \sigma_{\text{exc}}(T) = & 4\pi a_0^2 \frac{c_1}{(T/R)} \ln \left( 1 + \frac{T-c_2}{R} \right) \\ & \times [e^{-c_3/(T/R)} + c_4 e^{-c_5(T-c_2)/R(T/R)^2}]. \end{aligned} \quad (\text{A.5})$$

Here the different parameters have the same meaning as in Eq. (A.4).

Chouki's cross-sections for electron attachment, vibrational excitation and molecular dissociation were fitted to a formula, recommended

by Jackman et al. [33]:

$$\sigma_{\text{exc}}^{(j)}(T) = 4\pi a_0^2 R^2 \frac{f_j}{W_j^2} [1 - \zeta^{A_j}]^{B_j} \zeta^{\Omega_j} \quad (\text{A.6})$$

where  $\zeta = W_j/T$  and  $f_j$ ,  $W_j$ ,  $A_j$ ,  $B_j$  and  $\Omega_j$  are parameters that are characteristic of different excitation processes; the other quantities are those of Eq. (A.4). For the parameters, see again the publication by De Nardo et al. [27].

### A.3. Projectile-specific parameters

In order to perform the MC simulations in a way as close as possible to the experimental conditions, the MC code takes into account the energy spread of the projectile's beam and, at least in principle, also the radial distribution of the beam intensity. For the last, we assume a homogenous 1 mm-diameter cylindrical beam for protons and carbon ions produced in the accelerator, and a radial beam profile for alpha particles from an  $^{241}\text{Am}$  source (evaluated using the calculations according to Cunningham [34]). The energy spectrum of the different accelerator beams due to energy degradation in the scattering foil was determined using TRIM [16], and that of the alpha particles by direct measurements using a calibrated solid-state detector.

## References

- [1] A.J. Waker, *Radiat. Prot. Dosim.* 61 (1995) 297.
- [2] R. Schulte, V. Bashkurov, S. Shchemelinin, G. Garty, R. Chechik, A. Breskin, *Phys. Medica XVII (Suppl. 1)* (2001) 177.
- [3] H. Nikjoo, D.E. Charlton, Calculation of range distributions of damage to DNA by high- and low-LET radiations, in: A.F. Fuciarelli, J.D. Zimbrick (Eds.), *Radiation Damage in DNA: Structure/Function Relationships at Early Times*, Battell Press, Columbus, 1995, pp. 29–41.
- [4] A. Breskin, R. Chechik, P. Colautti, V. Conte, A. Pansky, S. Shchemelinin, G. Talpo, G. Tornielli, *Radiat. Prot. Dosim.* 61 (1995) 199.
- [5] L. De Nardo, P. Colautti, W.Y. Baek, B. Grosswendt, A. Alkaa, P. Segur, G. Tornielli, *Radiat. Prot. Dosim.* 99 (2002) 355.
- [6] U. Titt, A. Breskin, R. Chechik, V. Dangendorf, H. Schmidt-Böcking, H. Schumacher, *Nucl. Instr. and Meth. A* 416 (1998) 85.
- [7] S. Pszona, J. Kula, S. Marjanska, *Nucl. Instr. and Meth. A* 447 (2000) 601.
- [8] D. Chmielewski, N. Parmentier, J. Le Grand, Dispositif experimental en vue d'etudes dosimetriques au niveau du nanometre, *Proceedings of the Fourth Symposium on Microdosimetry*, EUR 5122 d-e-f, CEC, Luxemburg, 1973, p. 869.
- [9] Pszona, S. A track ion counter. *Proceedings of Fifth Symposium on Microdosimetry EUR 5452 d-e-f*, Published by the Commission of the European Communities, Luxemburg, 1976, p. 1107.
- [10] S. Shchemelinin, A. Breskin, R. Chechik, A. Pansky, P. Colautti, V. Conte, L. De Nardo, G. Tornielli, *Nucl. Instr. and Meth. A* 368 (1996) 859.
- [11] S. Shchemelinin, A. Breskin, R. Chechik, A. Pansky, P. Colautti, Anodosimeter based on single ion counting, in: D. Goodhead, P. O'Neel, H. Menzel (Eds.), *Microdosimetry—An Interdisciplinary Approach*, The Royal Society of Chemistry, Cambridge, 1997, pp. 375–378.
- [12] S. Shchemelinin, A. Breskin, R. Chechik, P. Colautti, R.W. Schulte, *Radiat. Prot. Dosim.* 82 (1999) 43.
- [13] G. Garty, S. Shchemelinin, A. Breskin, R. Chechik, I. Orion, G.P. Guedes, R. Schulte, V. Bashkurov, B. Grosswendt, *Radiat. Prot. Dosim.* 99 (2002) 325.
- [14] S. Shchemelinin, G. Garty, A. Breskin, R. Chechik, R.W. Schulte, *Nucl. Instr. and Meth. A* 477 (2002) 527.
- [15] S. Shchemelinin, S. Pszona, G. Garty, A. Breskin, R. Chechik, *Nucl. Instr. and Meth. A* 438 (1999) 447.
- [16] J.F. Ziegler, J.P. Biersack, U. Littmark, *The Stopping and Range of Ions in Solids*, Pergamon Press, New York, 1985.
- [17] A.F. Barbosa, G.P. Guedes, H.P. Lima Jr., *Nucl. Instr. and Meth. A* 477 (2002) 41.
- [18] J.F. Ward, The intracellular molecular damage which is dependent on radiation energy deposition patterns at the nanometer level, in: M.L. Mendelsohn (Ed.), *Genes, Cancer and Radiation Protection*, NCRP, Bethesda, MD, 1991, pp. 25–37.
- [19] J.F. Ward, *Radiat. Res.* 86 (1981) 185.
- [20] Stopping powers and ranges for protons and alpha particles. ICRU 49, International Commission on Radiation Units and Measurements, Bethesda, MD 20814, USA, 1993.
- [21] W.Y. Baek, B. Grosswendt, *Radiat. Prot. Dosim.* 52 (1994) 97.
- [22] M.E. Rudd, Y.K. Kim, D.H. Madison, J.W. Gallagher, *Rev. Mod. Phys.* 57 (1985) 965.
- [23] W.E. Wilson, L.H. Toburen, *Phys. Rev. A* 11 (1975) 1303.
- [24] Secondary electron spectra from charged particle interactions; ICRU 55, International Commission on Radiation Units and Measurements, Bethesda, MD 20814, USA, 1996.
- [25] W. Hwang, Y.K. Kim, M.E. Rudd, *J. Chem. Phys.* 104 (1996) 2956.
- [26] J.F. Ziegler, J.M. Manoyan, *Nucl. Instr. and Meth. B* 35 (1988) 215.

- [27] L. De Nardo, V. Conte, W.Y. Baek, B. Grosswendt, P. Colautti, G. Tornielli, Measurements and calculations of ionization cluster distributions in 20 nm size site (Report 175/2001), Istituto Nazionale di Fisica Nucleare—Laboratori Nazionali di Legnaro; Legnaro, Padova, Italy, 2001; *Radiat. Environ. Biophys.*, submitted for publication.
- [28] B. Grosswendt, E. Waibel, *Nucl. Instr. and Meth.* 155 (1978) 145.
- [29] A. Chouki, Détermination des sections efficaces de Collision électron-molécule dans l’Ethane, le Propane et l’Isobutane, Doctoral thesis, University Paul Sabatier, Toulouse, 1994.
- [30] A.E.S. Green, T. Sawada, *J. Atmos. Terr. Phys.* 34 (1972) 1719.
- [31] M.J. Berger, Spectrum of energy deposited by electrons in spherical regions, In: H.g. Ebert (Ed.), Proceedings of the Second Symposium on Microdosimetry, Report EUR 4452, Commission of the European Communities, Brussels, 1969, pp. 541–558.
- [32] C.B. Opal, E.C. Beaty, W.K. Peterson, *At. Data* 4 (1972) 209.
- [33] C.H. Jackman, R.H. Garvey, A.E.S. Green, *J. Geophys. Res.* 82 (1977) 5081.
- [34] H.E. Johns, J.R. Cunningham, *The physics of radiology*, 4th Edition, Charles C. Thomas publisher, 1983.